Nano Research

Open Access

Research Article

Forming mechanism of flexible microneedle array based on cooperation of jet printing and magnetic field-assisted stretching for wearable triboelectric pressure sensors

Zhen Chen[1], Hanxuan Lu[1], Haiming Wu[1], Gaoxiang He[1], Zhaoya Chen[1], Bei Wang[1], Shudong Yu[2], and Hui Li[1,3]

[1] *Guangdong Provincial Key Laboratory of Micro/Nano Optomechatronics Engineering, College of Mechatronics and Control Engineering, Shenzhen University, Shenzhen 518060, China*
[2] *School of Advanced Manufacturing, Shenzhen Campus of Sun Yat-sen University, Shenzhen 518107, China*
[3] *State Key Laboratory of Intelligent Manufacturing Equipment and Technology, Huazhong University of Science and Technology, Wuhan 430074, China*

Cite this article: *Nano Research*, **2026**, *19*, 94908415. https://doi.org/10.26599/NR.2026.94908415

ABSTRACT: Triboelectric pressure sensors with high sensitivity, broad linear range, and robust mechanical durability are critical for next-generation wearable human–machine interfaces. In this study, we present a microneedle-based triboelectric pressure sensor (MN-TPS) fabricated via a scalable additive manufacturing strategy that synergistically integrates jet printing and magnetic field-assisted stretching methods. This approach enables precise, controllable, and cost-effective fabrication of high-aspect-ratio microneedle array with tunable morphology. The optimized MN-TPS delivers an open-circuit voltage of 17.49 V under a 20 N force at 4 Hz, achieving a high-pressure sensitivity of 0.10 V/kPa at low regime (0–100 kPa) and maintaining linearity over an ultrawide range up to 400 kPa. Leveraging its fast response, we further integrate nine MN-TPS units into a wireless wearable interactive platform capable of real-time robotic control and dynamic trajectory recognition. This work bridges advanced microfabrication with practical human–machine interaction, establishing a versatile and generalizable platform for next-generation electronic skins, soft robotics, and intelligent wearable systems.

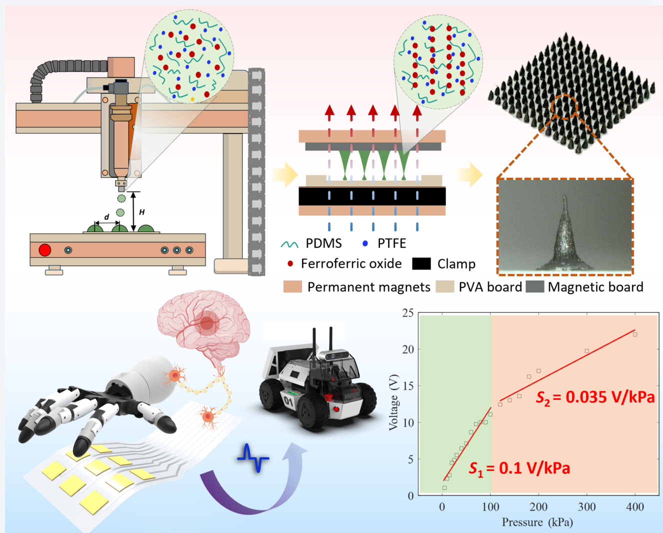

KEYWORDS: microneedle array, triboelectric nanogenerator, jet printing, magnetic field-assisted stretching, wearable sensor

1 Introduction

With the rapid and relentless advancement of the Internet of Things (IoT), flexible and wearable pressure sensors have emerged as a rapidly growing research frontier, owing to their inherent flexibility and lightweight design, and conformability to complex surface [1, 2]. These attributes have attracted tremendous attention due to the broad potential applications in robot motion tracking [3], human–machine interfaces [4], and environment condition monitoring [5], etc. Significant progress has been achieved in developing high-sensitivity, wide detection range, and large-scale pressure sensors based on different physical transduction mechanisms, such as piezoresistive [6], capacitive [7], triboelectric [8], and piezoelectric [9] effects. Amone these, triboelectric pressure sensors (TPS), based on a novel mechanical energy harvesting technology, are particularly favored for their advantages, such as simple structure, cost-effectiveness, environmental friendliness, self-powered sensing capability [10, 11].

Received: November 24, 2025; **Revised:** December 26, 2025
Accepted: January 6, 2026

Address correspondence to Hui Li, huili@szu.edu.cn; Shudong Yu, yushd6@mail.sysu.edu.cn

Moreover, the triboelectric effect originates from contact between two dissimilar materials, offering a vast design space for selecting optimal material pairs tailored to specific sensing requirements [12, 13].

To enhance the spatial interaction and pressure sensitivity of TPSs, it is of vital importance to reduce the surface stiffness of non-ideal planar triboelectric films and enlarge the contact area between triboelectric layers during the triboelectrification process [14, 15]. To achieve this, extensive efforts have been devoted to engineering protruding microstructures on sensor surfaces, such as pyramid array [16, 17], micro-bowls [18], microcones [19], micro domes [20], to facilitate localized stress concentration and improve charge transfer. Among these, microneedles (MNs) have emerged as a promising architecture for triboelectric pressure sensor due to their superior mechanical compliance, high aspect ratio, and enhanced interfacial interaction [21]. The unique operating mechanism of MNs also provides a promising pathway to simultaneously enhance sensitivity and extend the linear response range of the sensor. For instance, Chen et al. [22] developed a bendable microneedle array based triboelectric pressure sensor, and demonstrated that its output performance could be significantly enhanced via the unique bending-friction-deformation mechanism of MNs. To produce excellent MNs, various fabrication techniques have been explored [23], including lithography with wet or dry etching [24], laser cutting [25, 26], micromachining [27], wire electrode cutting [28], molding method [15, 29], etc. However, most of these approaches often suffer from drawbacks, such as high production costs, reliance on expensive equipment, low processing efficiency, and limited scalability, making them less suitable for mass production [30]. Consequently, there remains an urgent demand for a simpler, more cost-effective, and scalable fabrication strategy capable of producing robust, high-performance MN structures without compromising device functionality.

Recently, additive manufacturing (AM) has emerged as a revolutionary technology, attracting considerable attention from both industry and academic sectors due to its short design-to-production cycle, low cost, and efficient material utilization [31]. A variety of AM techniques, such as direct ink writing [19, 32], electrospinning-based printing [33], stereolithography [34], and fused deposition modeling [35], have been employed to fabricate MNs. However, to further enhance the output performance and enable specialized lightweight designs, there is a growing demand for advanced fabrication methods and surface architectures. These often involve intricate geometries and periodically repeating units [36]. Therefore, there is an urgent demand to develop and integrate novel additive manufacturing approaches that enable rapid, cost-effective, and scalable production of such complex microstructures.

This study presents a well-designed wearable TPS for human–machine interaction, featuring with flexible MN array as the active triboelectric layer. The MN array is fabricated through cooperation of jet printing and magnetic field-assisted stretching method (CJMS), which offers compelling advantages including low cost, scalability for mass production, full functional integration, and exceptional structural uniformity. We systematically evaluated the output performance of microneedle-based triboelectric pressure sensor (MN-TPS), demonstrating that optimized fabrication parameters and tailored MN geometry significantly enhance interfacial contact area, thereby improving both sensitivity and linear response range. To ensure practical applicability, we comprehensively evaluated key performance indicators such as durability, sensitivity and pressure range. Furthermore, we developed a wearable controller capable of real-time motion trajectory perception, spatial localization, and precise robotic manipulation. This research introduces an efficient strategy to streamline the design-to-fabrication cycle of wearable sensors and highlights their strong potential in emerging applications such as real-time tactile sensing and intelligent human–robot interfaces.

2 Experimental section and characterization

2.1 Materials

Polydimethylsiloxane (PDMS, Sylgard 184, Dow Corning, USA) and curing agent were mixed at a weight ratio of 10:1 as the base elastomer. To formulate a homogeneous and printable magnetic ink, iron nanoparticles (average diameter: 200 nm, Hebei Jincai Shengte Metal Materials Co., China), nanoscale polytetrafluoroethylene (PTFE, average diameter: 5 nm, Zhonglian Plastic Chemical Co., China), and PDMS were combined at varying ratios using a planetary mixer (AR-100, Thinky, Japan) at 2000 rpm for 3 min, followed by vacuum deaeration for an additional 1 min. This process demonstrated uniform dispersion of the fillers and optimal tuning of both magnetic responsiveness and rheological properties for printability.

2.2 Fabrication of the MN array

Human skin is a sophisticated sensory system composed of multiple layers, including epidermis, dermis, and hypodermis, along with numerous embedded mechanoreceptors, as shown in Fig. 1(a). Hair follicles penetrate through the skin and function as sensitive force detectors. Tiny mechanical stimuli can induce deformations in the hair, which are then transmitted to Aβ afferents as tactile signals. This elegant biological design has inspired the development of hair-mimetic architectures for advanced wearable sensors. Inspired by this natural architecture, we adopted hair-like microneedles as the dielectric layer in triboelectric pressure sensors. Figure 1(b) presents the schematic diagram of the MNs fabrication process. The fabrication process consists of three key steps, including jet printing, magnetic field-assisted stretching and thermal curing. First, the prepared magnetic ink (mass ratio of Fe/PTFE/PDMS is 12%:30%:58%) is dispensed via a piezoelectric jetting system to form microcone array on the substrate. To optimize the printing efficiency and cone morphology, several fabrication parameters are carefully controlled, including nozzle-to-substrate distance, driving voltage, printing velocity, etc. Notably, the jet printing experimental setup comprises a three-dimensional motion platform, a piezoelectric jetting dispenser, a high-speed camera, a light source, and a piezoelectric controller. The piezoelectric jetting dispenser serves as the core component of this system and consists of a piezoelectric stack, transmission lever, return spring, needle, nozzle tip, and syringe [19]. A nozzle tip with an inner diameter of 60 μm is employed for jet printing. Under controlled conditions, ejected droplets spontaneously self-assemble into well-defined microcones upon contact with the substrate. In the second step, the uncured microcone array is exposed to a tunable external magnetic field generated by a pair of parallel NdFeB permanent magnets (Meici Magnetic Components Co., China). The optimal magnetic field strength is 300 mT. The inter-magnet distance is precisely adjusted via a linear motor. As the top substrate moves down to gently contact the microcone tips and is

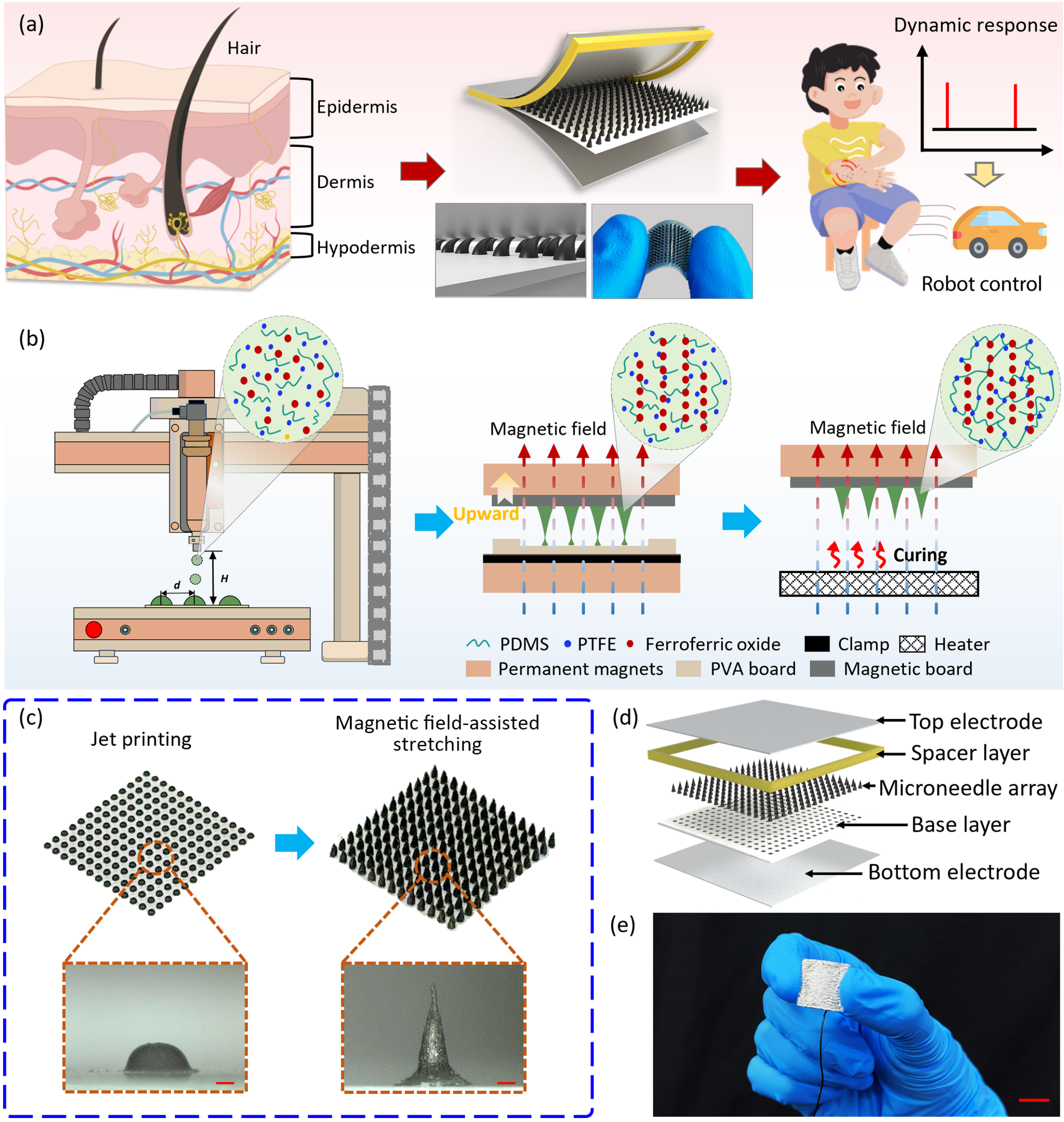

Figure 1 Fabrication of MN-TPS. (a) Concept, design, and performances of MN-TPS. (b) The schematic diagram of the experimental setup and fabrication process of MN array. (c) Optical photographs of printed patterns with and w/o MNs. (d) Structure of MN-TPS. Scale bar: 200 μm. (e) A photograph of MN-TPS, with the dimension of 15 mm in length and 15 mm in width for MN array. Scale bar: 5 mm.

then retracted at the constant velocity of 1 mm/s, the soft cones are elongated under the combined action of magnetic force and mechanical stretching. This magnetic field-assisted stretching process enables precise elongation and alignment of the MNs. Detailed fabrication parameters are provided in Table S1 in the Electronic Supplementary Material (ESM). These parameters were selected based on a systematic trade-off among morphological quality, structural integrity, and process robustness. Specifically, 300 mT magnetic field was applied to promote pronounced particle elongation. Stretching velocity of 1 mm/s was selected to reach the saturation point of MN height under stable conditions. Compression distance of 0.4 mm could maximize MN height as well. 20 droplets ensured sufficient material for reliable formation of high MN. This parameter set establishes a robust protocol for MN array fabrication. Finally, the structured film undergoes thermal curing at ~ 80 °C for 1 h to solidify the MN array, ensuring robust mechanical integrity and long-term stability. Figure 1(c) compares MN array fabricated with and without magnetic field-assisted stretching. Both types exhibit excellent uniformity and consistency across the substrate, and dimensions can be precisely tuned by adjusting the printing parameters.

2.3 Preparation of the wearable TPS

Figure 1(d) shows the configuration of the MN-TPS, which comprises a negative triboelectric layer (PDMS base layer and MN array), two electrodes, and insulating spacers. Conductive Al foil

(Ningbo ASH- BURN Aluminum Foil Products Co., Ltd., China) was used as the negative electrode and fixed onto the rigid workstation. The PDMS layer was directly printed onto the electrode to form the base layer. Subsequently, MN array was fabricated on the top using the CJMS method. Another aluminum foil was severed as the positive electrode. To assemble the MN-TPS, these two sections were bonded onto flexible PVC films and aligned in a face-to-face configuration, separated by a spacer with thickness of 2 mm. Copper wires were individually connected to each electrode to transfer the generated electrical signal to the external circuit. The photograph of TPS is shown in Fig. 1(e).

The MN-TPS was operated using a custom-built programmable linear motor workstation in a vertically oriented contact-separation mode, with varying compressive forces (1 to 40 N) and excitation frequencies (1 to 4 Hz). The output performance was evaluated by measuring the open-circuit voltage, short-circuit current, and transferred charge using an electrometer (Model 6514, Keithley).

2.4 Characterization

The formation process of the MN was monitored and recorded using a high-speed camera (M230M, Revealer AgileDevice) equipped with an integrated light source. The three-dimensional morphology of the MN was characterized using a super-depth digital microscope (VHX-2000, Keyence, Japan). Mechanical force applied during testing was measured with a high-resolution strain gauge (M3552C, Sunrise Instruments, China), which was mounted on the bottom of the sensor platform. The magnetic field intensity was measured using a Teslameter (Victor Instruments 862B). Rheological properties of the printing inks were evaluated using a rotational rheometer (Anton Paar MCR 92) fitted with a 40 mm cone-plate geometry (cone truncation gap: 50 μm). Viscosity was measured in steady shear mode over a shear rate range from 0.1 to 100 s^{-1}.

3 Results and discussion

Figure 2(a) shows the image sequences and a corresponding schematic illustration of a single-pulse jet printing cycle used to fabricate microcone structures. Initially, the printable ink is confined within the printing head. When the piezoelectric stack is de-energized, a tappet-spring mechanism generates an abrupt pressure surge, propelling the ink through the nozzle orifice. Once ejection, the droplet extends into a continuous liquid column between the nozzle and the substrate, sustained by the ink's inertia and high viscosity [37]. Once the voltage pulse terminates, the driving force dissipates, rendering the liquid column unstable. Under the combined influence of gravity, inertia force and substrate adhesion, the column fractures near its midpoint. The upper portion retracts back to the nozzle, while the lower segment detaches and falls onto the nascent cone, rapidly coalescing to form a cone-shaped precursor structure. With successive droplet depositions, ink is accumulated on the substrate, gradually building a microcone structure. This process is highly controllable, and the final structure size increases progressively with the number of ejected droplets, enabling precise tuning of geometry.

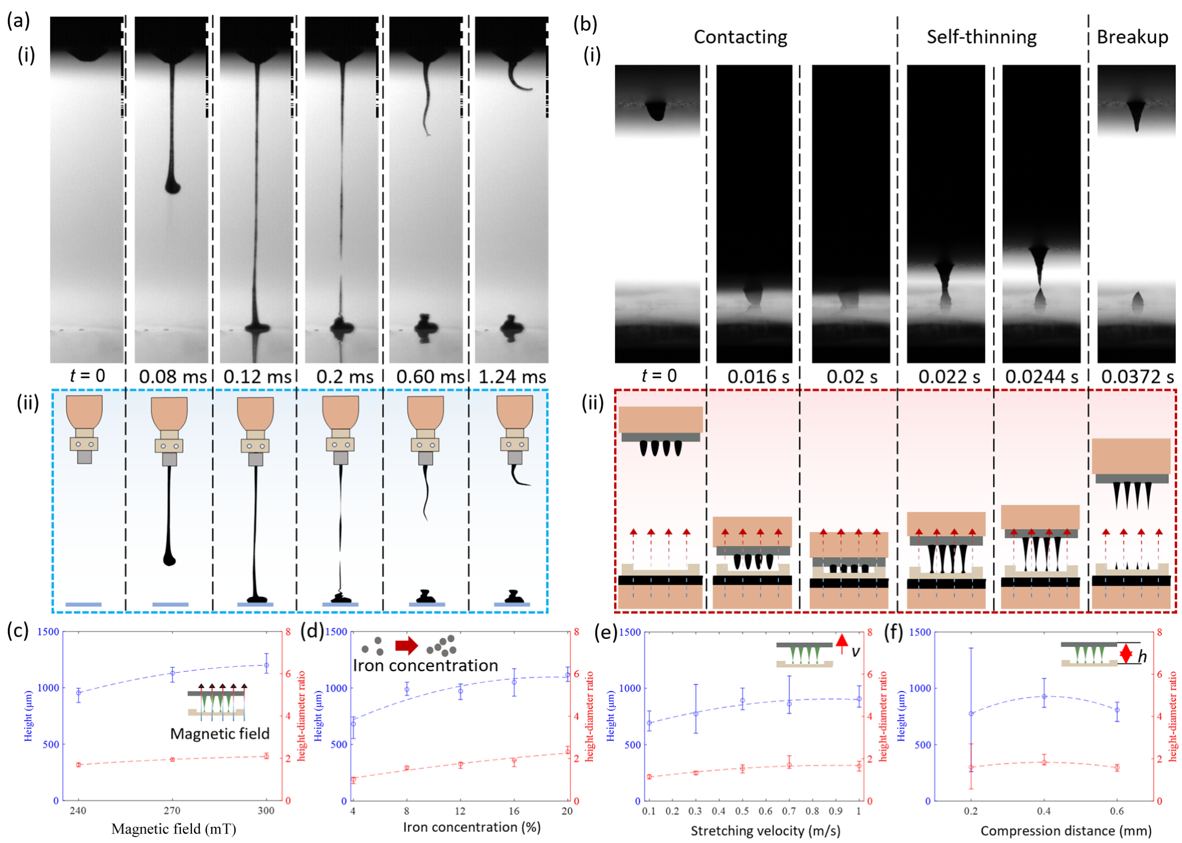

Figure 2 Fabrication process and characterization of the MN array. (a) Image sequences and schematic illustration of a single-pulse jet printing process for under high-speed camera. (b) Image sequences and schematic illustration of the magnetic field-assisted stretching process under high-speed camera. (c) Influence of magnetic field intensity on the shape parameters of MN. Data are presented as the mean and standard deviation (n = 8). (d) Influence of iron concentration on the shape parameters of MN. Data are presented as the mean and standard deviation (n = 8). (e) Influence of stretching velocity on the shape parameters of MN. Data are presented as the mean and standard deviation (n = 8). (f) Influence of compression distance on the shape parameters of MN. Data are presented as the mean and standard deviation (n = 8).

Figure 2(b) presents the image sequences and a schematic diagram of the magnetic field-assisted stretching process for MN. The forming of MNs can be divided into three distinct states, including contacting, self-thinning, and breakup. Initially, the sample with freshly printed microcone structure is mounted upside-down on the top substrate in a magnetic field environment. This top substrate is then lowered until the tips of microcone make contact with the bottom substrate. Subsequently, the top substrate is moved upward at a constant velocity, and a liquid bridge forms between the two substrates due to the viscoelasticity and surface adhesion of the uncured material. As separation continues, the liquid bridge undergoes extensional deformation, entering an elasto-capillary self-thinning regime. During this phase, the bridge maintains a dynamically stable, waist-like profile under a balance of competing forces, stretching force, magnetic force, surface tension, gravity, and viscous resistance. When further elongation, stress concentrates at the neck of the liquid bridge. Once the local tensile stress exceeds the rupture threshold of the material, capillary instability triggers rapid breakup. The bridge fractures into two segments, with one remaining on the bottom substrate, while the other anchoring to the top substrate. Immediately following breakup, a sharp, high-aspect-ratio liquid MN is self-assembled on the pillar tip, stabilized *in situ* by the external magnetic field. Within the ink, magnetic nanoparticle chains and PTFE-reinforced networks act as internal scaffolds, preventing recoil and suppressing retraction of the elongated tip. When the vertical forces, including magnetic attraction force, surface tension, and gravity, reach a new equilibrium, the fabrication process is complete, and the fine MN structure is preserved under the magnetic field. Finally, the structure is thermally cured, permanently fixing the shape and yielding a robust, sharp microneedle on the top substrate.

Magnetic field intensity significantly influences MN formation, as shown in Fig. 2(c). Error bars represent the standard deviation from independent experiments. Generally, higher magnetic field strength leads to greater MN height. The reason is that the external magnetic field magnetizes the ferromagnetic nanoparticles within the polymer matrix, inducing dipole–dipole interactions. These interactions drive the alignment of particles into chains, which further aggregate to minimize the system's magnetic potential energy. This chain growth promotes anisotropic, longitudinal elongation of the liquid bridge during stretching, thereby enhancing the final aspect ratio of the cured microneedles [22].

Figure 2(d) shows the influence of iron nanoparticle content on the morphological parameters of the MNs. As the iron nanoparticle concentration increases from 4 wt.% to 20 wt.%, the height of MN gradually increases from 682 to 1117 μm. Correspondingly, the height-diameter ratio also exhibits a gradual upward trend. This enhancement is attributed to the increased magnetic responsiveness of the printable ink. As the iron nanoparticle content increases, the elongation force is strengthened as well under the external magnetic field. Figure S1 in the ESM shows the viscosity of the printable ink with various iron contents. Figure S2 in the ESM illustrates the effect of droplet quantity on the geometry of the MNs. As expected, the height of the MN increases approximately linearly with droplet quantity, ranging from 10 to 60 droplets. In contrast, the base diameter increases proportionally, resulting in a nearly constant height-diameter ratio across all quantities. This indicates scalable, geometry-preserving growth through droplet accumulation.

In addition to magnetic field parameters, the mechanical stretching conditions also significantly influence MN formation. As shown in Fig. 2(e), increasing the stretching velocity from 0.1 to 1 mm/s leads to a corresponding increase in MN height (from 692 to 907 μm). This trend arises from the enhanced inertial forces generated during faster substrate retraction, which overcome the surface tension of the uncured ink. These forces promote sustained elongation of the liquid bridge along the stretching direction, thereby stabilizing the formation of MNs with a certain height-diameter ratio and resulting in larger final dimensions as the velocity increases.

Another critical parameter is the compression distance, which indicates the initial distance between the top and bottom substrates. As can be seen in Fig. 2(f), when the compression distance rises from 0.2 to 0.6 mm, the MN height first increases to the maximum value of 927 μm at the compression distance of 0.4 mm and then decreases. This phenomenon is reasonable, and the variation can be attributed to the following two factors. At small compression distances (0.2 mm), the microcone structure is compressed by the two substrates, causing lateral outflow of the uncured ink and consequent widening of the base diameter. Thus, more materials are adhered to the substrates, yielding larger viscous force and impeding the MN generation. Conversely, when the compression distance is large (0.6 mm), only the tip of the microcone structure contacts with the bottom substrate. Limited contact area restricts material adhesion, thereby providing insufficient viscous force to sustain stable liquid bridge formation during stretching. Consequently, the elongation capability is diminished, producing shorter and blunter microneedles.

Figure 3(a) shows the working principle of the MN-TPS in contact-separation mode. When an external force is applied, the microcone-structured negative triboelectric layer contacts the Al film. Electrons transfer from the Al to the PDMS surface due to triboelectrification, creating opposite charges on the two layers. As the layers separate, the electrode under the PDMS induces positive charges, causing electrons to flow from the bottom electrode to the Al film through the external circuit. This generates a current. When the force is fully released, the charge density reaches its peak. As the layers come back into contact, electrons flow in the reverse direction, completing the alternating current cycle. This continuous electron flow converts mechanical energy into electrical energy. Moreover, to verify the working principle of MN, high speed camera was used to capture and measure the contact-separation process. As can be seen in Fig. 3(b), when the top electrode moves downwards, inducing the forced deformation for MNs obviously (Movie S1 and Fig. S6 in the ESM).

The output performance of MN-TPS is mainly governed by the micro structure and tribopolarity of the triboelectric layers [38]. Figure 3(c) compares the output performance of MN-TPS between MNs and microcones under the identical operation condition of 4 Hz frequency and 20 N external force. It is found that the output voltage for MN-TPS can achieve 17.49 V, which is 1.26 times larger than that with microcones. This enhancement may be attributed to two main factors, including the foundational increase in contact area and the unique dynamic deformation of the MNs. Unlike rigid microcones that undergo simple compression, MNs exhibit significant elastic bending under applied force. This bending mechanism can simultaneously sustain continuous MN sidewall friction and generate microscopic air gaps. The triboelectric effect triggered by these dynamic gaps can produce additional localized electric fields, which substantially enhance surface charge density and overall charge transfer efficiency [39]. Figure S3 in the ESM

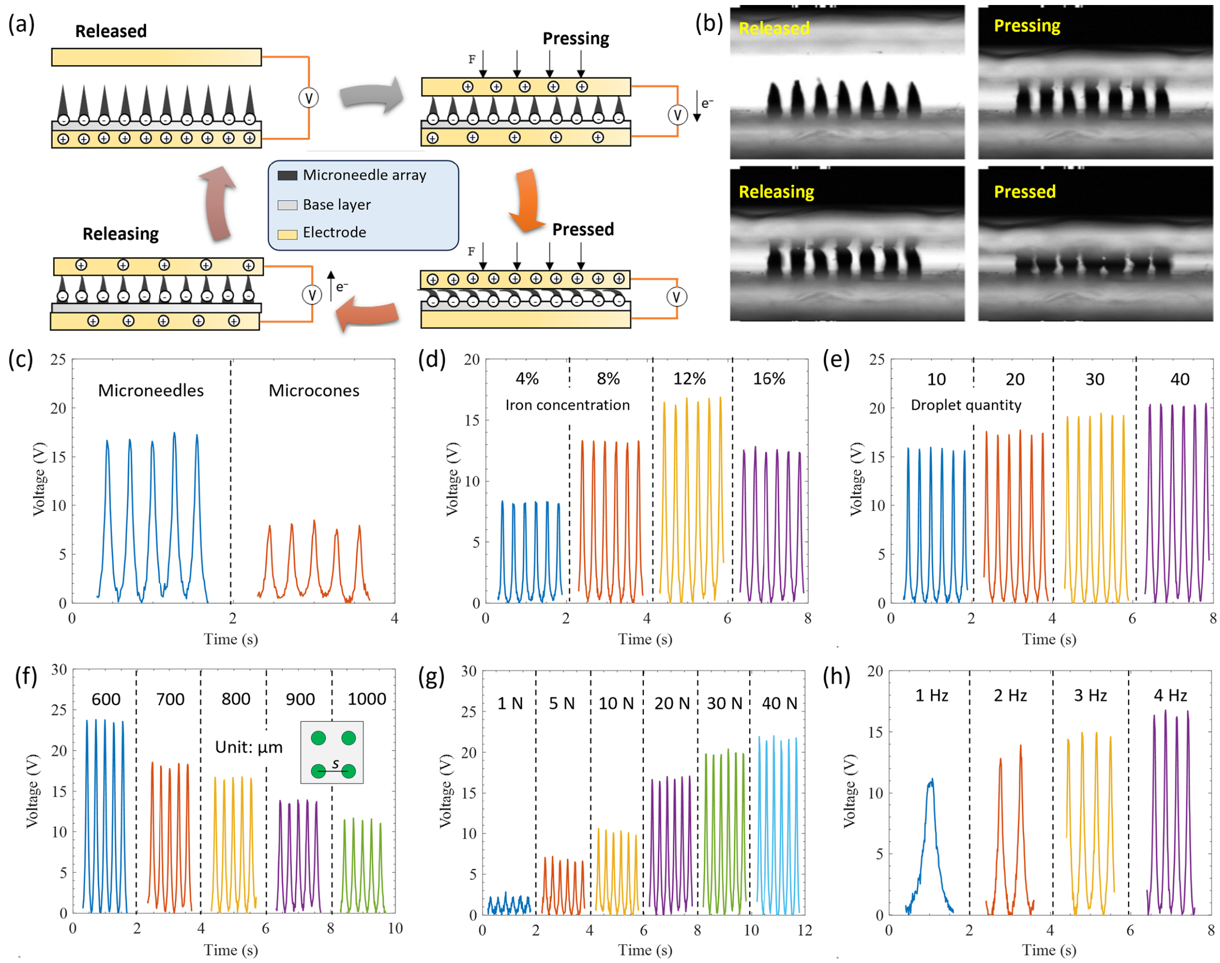

Figure 3 The electrical characteristic generated by MN-TPS. (a) Working principle of MN-TPS at contact-separation mode. (b) Image sequence of operated MN-TPS under high speed camera at 5 N for one contact-separation period. (c) Comparison of output performances for TPS with MNs and microcones. (d) Output performance of MN-TPSs with various iron nanoparticle contents. (e) Output performance of MN-TPSs with different droplet quantity. (f) Output performance of MN-TPSs with different MN spacings. (g) Influence of vibration force for output voltage. (h) Influence of vibration frequency for output voltage. Data points represent discrete measurements.

shows the short-circuit current and transferred charges of these two TPS types. Note that MN-TPS shows better output performance.

To optimize performance, key fabrication parameters affecting contact efficiency were systematically studied, including iron concentration, droplet quantity, and MN spacing. Figure 3(d) shows the effect of iron concentrations on the output performance at an applied force of 20 N and a frequency of 4 Hz. As the iron powder content increased gradually from 4% to 12%, the output voltage significantly increased from 8.3 to 16.8 V. This performance enhancement is primarily attributed to the increased micro-needle height resulting from higher iron powder loading, which enables greater deformation of the flexible micro-needle array during the contact-separation process with aluminum foil, thereby effectively enhancing the accumulation and transfer efficiency of triboelectric charges. However, when the iron powder content was further increased to 16%, the output voltage decreased to 12.6 V. This performance degradation may be attributed to two main factors. First, higher MNs tend to bend under compression, converting mechanical energy into elastic deformation rather than effective contact electrification, and then reducing the output performance [39]. Second, an appropriate amount of Fe can enhance the capacitance of PDMS, thereby increasing the output voltage. But excessive Fe content degrades the dielectric properties of the ink, suppressing triboelectric charge generation and ultimately reducing voltage output [40].

Droplet quantity also influences the output performance of MN-TPS. As shown in Fig. 3(e), when the droplet number increases from 10 to 40, the open-circuit voltage gradually increases. This trend can be attributed to two factors. First, a higher droplet quantity means more material is deposited on the substrate, resulting in taller and larger MN with increased surface area. The more complex surface structure enhances contact area during operation, thereby boosting triboelectric charge generation. Similarly, Xie et al. [41] also fabricated microstructures on the triboelectric layer. They also found that the thermoplastic polyurethane foam with more complicated bumps and valleys would be beneficial for the enhancement of the output performance for TENG, and higher triboelectric output voltage could be achieved as with the increase of the specific surface. Secondly, as with the increase of the additives (PTFE and Fe) in the printed inks, more charges can be gained during the contacting with the positive electrode. We also compare the output performance of PDMS, PDMS/Fe, PDMS/PTFE, and PDMS/Fe/PTFE as triboelectric layers in Fig. S7 in the ESM. The results show that both PTFE and Fe incorporation can enhance the output performance of the TPS, with the PDMS/Fe/PTFE composite achieving the highest output voltage as expected.

The density of MNs on the negative layer also affects the output performance of the MN-TPS. To evaluate this effect, MNs with different spacings were prepared. As shown in Fig. 3(f), when the spacing between cones increases from 600 to 1000 μm, the output voltage significantly decreases from 23.8 to 11.6 V, in which data points represent discrete measurements. This reduction is because higher MN density provides a larger effective contact area under the same applied force, enabling more triboelectric charge generation on the surface.

Furthermore, we evaluated the output performance of the MN-TPS under varying mechanical excitation conditions. Figure 3(g) shows the effect of applied force on the output voltage, where data points represent discrete measurements. As the force increases from 1 to 40 N, the voltage rises from 2.2 to 21.6 V. This is because a larger applied force compresses the soft microstructures more effectively, increasing the contact area between the triboelectric layers. As a result, more charges are generated, leading to higher charge density and enhanced output. Figure 3(h) presents the effect of operation frequency (ranging from 1 to 4 Hz) on the output voltage. A slight increase in voltage is observed with higher frequency, which is expected since a faster contact-separation cycle can induce a greater rate of charge transfer in each cycle.

The durability of MN-TPS, fabricated using an optimized stretching velocity of 1 mm/s and a compression distance of 0.4 mm, was evaluated to assess its potential for practical applications. As shown in Fig. 4(a), the stability performance of MN-TPS was measured at a frequency of 4 Hz and an applied force of 20 N. After being stored in ambient condition (approximately 24 °C and 60% relative humidity) for four weeks, there is a slight variation in the electrical output response, indicating good environmental stability. The long-term reliability was measured as well, as shown in Fig. 4(b). It is found that after working in contact-separation mode for over 8000 cycles continuously, there is no evident change in the output voltage.

To evaluate the sensitivity of the MN-TPS, the relationship between applied pressure and output voltage was investigated. As shown in Fig. 4(c), the normalized voltage increases linearly with pressure over the range of 0–400 kPa. Specifically, the sensitivity is approximately 0.1 V/kPa in the low-pressure range (0–100 kPa), enabling high responsiveness to light mechanical stimuli. At higher pressures, the sensitivity decreases to about 0.035 V/kPa. In addition, the sensitivity and the width of the linear range of previously reported triboelectric pressure sensors are investigated and summarized, as shown in Fig. 4(d). Obviously, the MN-TPS manifests the widest linear range and maintaining competitive sensitivity [42–62]. A detailed summary is presented in Table S2 in the ESM to provide a more comprehensive comparison of key metrics, including structure type, sensitivity, linear range, and durability. This characteristic arises from a trade-off in which the MN sacrifices ultimate sensitivity in favor of an exceptionally broad linear response range. This wide linearity offers a significant advantage for applications in gait analysis and robotic gripping. This robust performance highlights the device's promise for real-world applications.

Figure 4(e) shows the output voltage and power of the MN-TPS across various load resistances, measured under a frequency of 4 Hz and a vertical force of 20 N. The output voltage rises with increasing resistance and saturates at approximately 17 V. The maximum power of 1.74 μW is achieved at a load resistance of 100 MΩ, indicating optimal impedance matching at this value. Figure S4 in the ESM demonstrates the charging performance of the MN-TPS using capacitors with different capacitances, including 0.22, 1, 2.2, and 4.7 μF. The device charges the 0.22 μF capacitor to 4.8 V within 4.5 s. Larger capacitors take longer to charge but store more energy. This confirms that while smaller capacitors enable faster voltage buildup, larger ones offer superior energy storage capacity under continuous mechanical excitation.

To further demonstrate its application as a wearable controller for human–machine interaction, a versatile interactive platform based on MN-TPSs was developed for real-time robotic control. A schematic diagram of the wireless control system was presented in Fig. 5(a). The system comprises an MN-TPS-based control

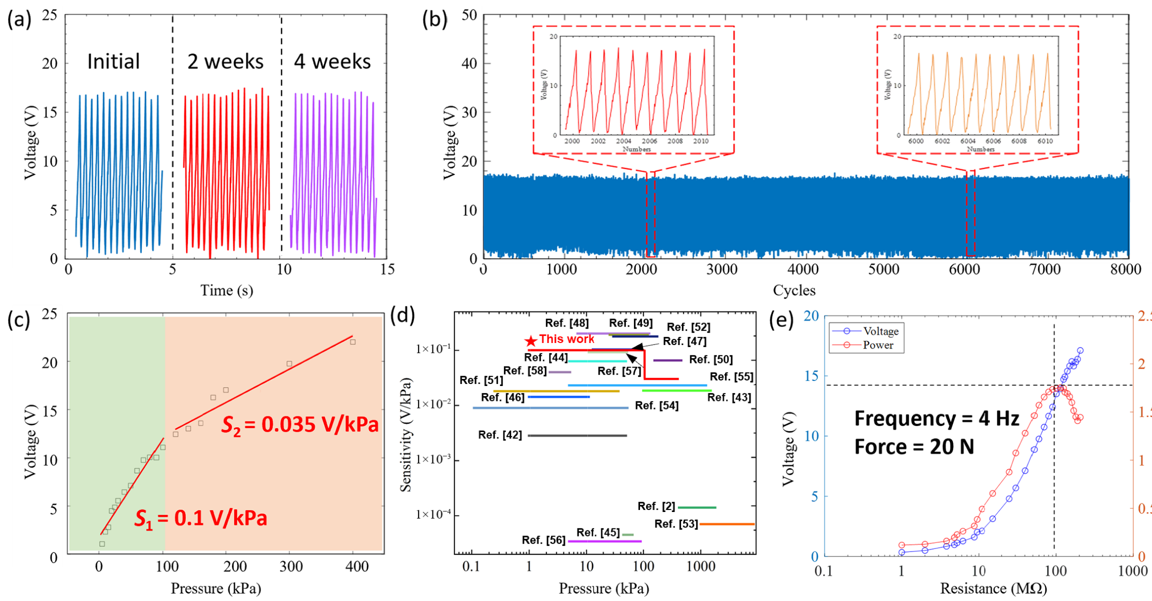

Figure 4 Characterizations of the MN-TPS. (a) Mechanical endurance test of MN-TPS in four weeks. (b) Stability measurement under continuous compressive force for 8000 cycles. (c) Output voltage response to a wide range of pressure. (d) Comparison in the sensitivity and linear range of TPS. (e) The output voltage and power density of the MN-TPS with various loads.

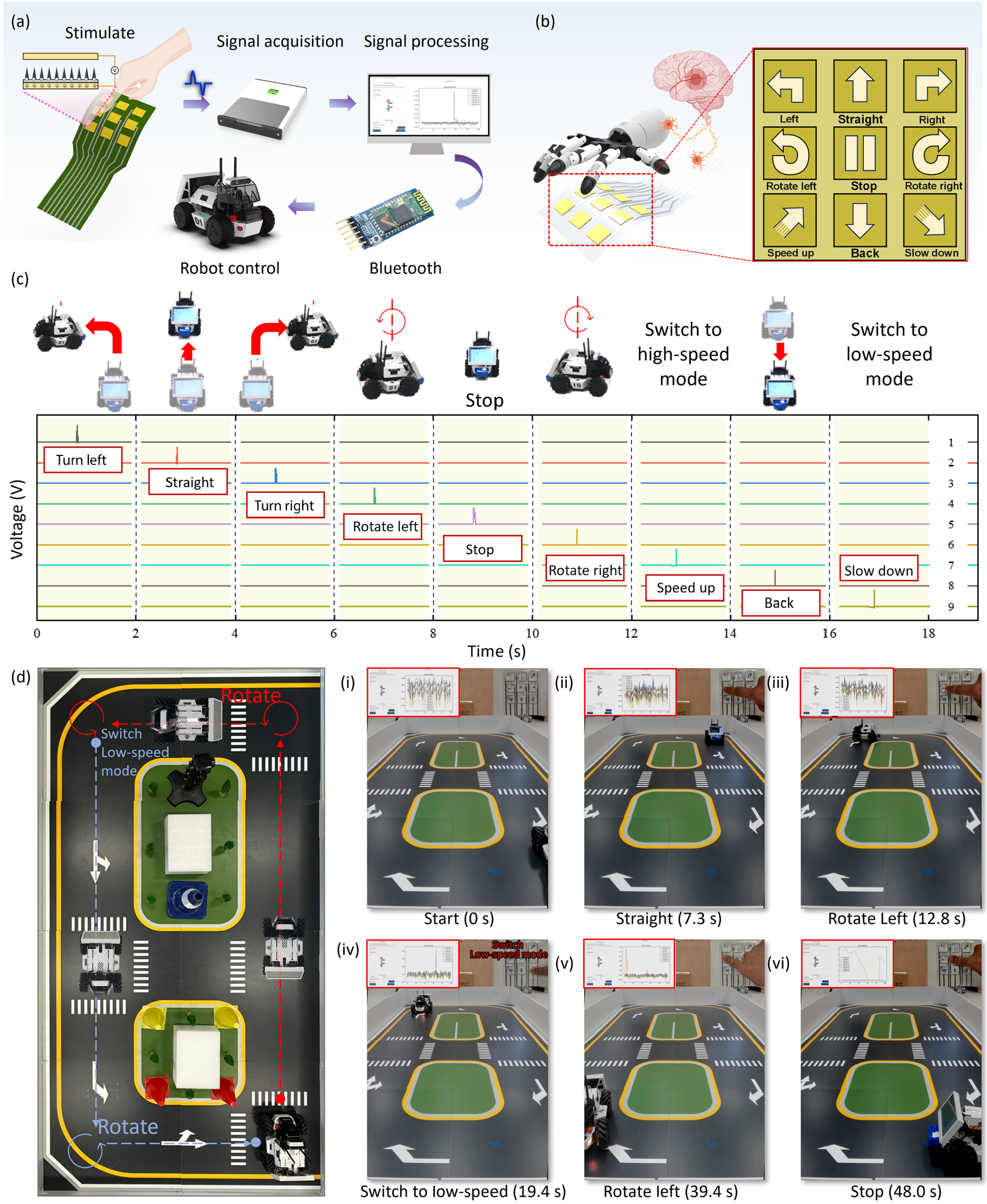

Figure 5 Application of MN-TPS based wearable interactive platform for robot control. (a) Working principle of MN-TPS based wearable interactive platform for robot manipulation. A pressing signal can be converted into a trigger signal to control the appliances. (b) Schematic diagram of the interactive platform with nine control buttons for specific functions. (c) Output signal waveforms from each of the nine specific-function buttons. (d) Screenshot of the wirelessly controlled smart mobile robot performing the programmed task.

interface, a data acquisition system (DAQ, USB-6349, National Instruments), a signal processing computer, and a miniature mobile robot equipped with Mecanum wheels (AgileX LIMO, AgileX Robotics). Nine MN-TPSs were integrated as tactile buttons on the interactive platform. Their output voltage signals were simultaneously captured via the multichannel DAQ system and processed in real time on the host computer to suppress environmental noise. The signals pass through a 0.1–15 Hz zero-phase band-pass filter to extract the effective frequency band. Then the adaptive notch filters at 50 Hz and its harmonics are applied to eliminate powerline interference. After analog pulse signals were converted into square wave pulses, corresponding command signals were transmitted wirelessly via a Bluetooth module, enabling remote control of the mobile robot.

We first demonstrate the platform's ability to identify the spatial location of a contact event. By continuously monitoring the voltage signals from all nine channels in real time, the trajectory of a moving touch can be accurately reconstructed. As shown in Fig. S5 in the ESM, with a schematic diagram depicting the "S", "Z", and "U" paths, the corresponding output signals from nine channels clearly exhibited a distinct and sequential activation. This precise spatiotemporal correlation between the input trajectories and the multi-channel signal output confirms the capability for dynamic touch recognition.

Subsequently, Fig. 5(b) illustrates the functional mapping of the nine buttons, including forward/backward motion, left/right rotation, turning left/right, speed adjustment (acceleration/deceleration), and emergency stop. As shown in Fig. 5(c), when specific buttons are pressed, distinct voltage signals are generated and recorded in real time, triggering corresponding actions in the robot. Figure 5(d) presents a screenshot of the robot executing the programmed task. The entire control sequence is as follows: (i) initiate movement and advance at high speed; (ii) rotate left at 7.3 s; (iii) move forward and rotate left at 12.8 s; (iv) rotate left and switch to low-speed mode at 19.4 s; (v) rotate left and continue straight at 39.4 s; (vi) return to the starting point and stop at 48.0 s. The complete control process, robot motion and voltage signals are also provided in Movie S2 in the ESM. These results demonstrate the successful implementation of wireless control using the MN-TPS-based interactive platform, highlighting its promising potential for applications in artificial robotics, autonomous systems, unmanned vehicles, and unmanned aerial vehicles.

4 Conclusion

In summary, we have developed a MN-TPS for high-fidelity tactile perception and human–machine interaction. An additive manufacturing approach, cooperation of jet printing and magnetic field-assisted stretching method, was established to fabricate the uniform, high-aspect-ratio MN array in a controllable, cost-effective, and scalable manner. The MN-TPS delivers an output voltage of 17.49 V at the external force of 20 N and operation frequency of 4 Hz, which achieves instantaneous peak power of 1.74 μW, high pressure sensitivity of 0.1 V/kPa at low pressure and linear detection range (0–400 kPa). Meanwhile, MN-TPS exhibited excellent durability, reliability, and enabled the achievement of real-time sensing. We further implemented a wearable MN-based control interface that seamlessly integrates tactile input with interactive functionality. This system enables precise navigation of a smart mobile robot and accurate handwriting recognition. Consequently, this work provides a new manufacturing strategy for developing wearable TPS, demonstrating significant potential in wearable electronics and showing a broad spectrum of promising future applications in human–machine interaction.

In addition, although the CJMS method is scalable and cost-effective, it has limitations that affect its practical use and require further improvement. It relies on magnetic nanocomposites, which restricts material choices. Scaling up to large sensors demands advanced systems to maintain a uniform magnetic field and ensure substrate alignment during the dynamic stretching process. Moreover, as a planar fabrication technique, it seems difficult to conform to curved or complex 3D surfaces. Therefore, more effort is needed to transition this promising approach toward reliable manufacturing for wearable electronics.

Electronic Supplementary Material: Supplementary material (viscosity of different inks, influence of droplet quantity on the shape parameters of MN, short-circuit current and transferred charges of the two TPS types, charging performance for the MN-TPS, the capability of the platform to identify the spatial location of a contact event, electrostatic simulation of the electromechanical coupling in a bending microneedle, triboelectric output performances of pure PDMS, PDMS/PTFE, PDMS/Fe, and PDMS/Fe/PTFE composite films, and detailed fabrication parameters and pressure sensitivity comparison) is available in the online version of this article at https://doi.org/10.26599/NR.2026.94908415.

Data availability

All data needed to support the conclusions in the paper are presented in the manuscript and the Electronic Supplementary Material. Additional data related to this paper may be requested from the corresponding author upon request.

Acknowledgement

The authors gratefully acknowledge the projects supported by the National Key Research and Development Program of China (No. 2024YFB3213600), the National Natural Science Foundation of China (No. 52405329), and Shenzhen Science and Technology Program (Nos. JCYJ20220818100001002 and JCYJ20250604182636049).

Declaration of competing interest

The authors declare that they have no known competing financial interests or personal relationships that could have appeared to influence the work reported in this paper.

Author contribution statement

Z. C.: Methodology, experimental design, formal analysis, writing manuscript. H. X. L.: Conceptualization, investigation, software. H. M. W.: Data curation, investigation. G. X. H.: Visualization, formal analysis. Z. Y. C.: Investigation, validation. B. W.: Data curation, investigation. S. D. Y.: Resources. H. L.: Funding acquisition, methodology, supervision, writing – review & editing.

Use of AI statement

None.

References

[1] Zhang, Q.; Jin, T.; Cai, J. G.; Xu, L.; He, T. Y. Y.; Wang, T. H.; Tian, Y. Z.; Li, L.; Peng, Y.; Lee, C. Wearable triboelectric sensors enabled gait analysis and waist motion capture for IoT-based smart healthcare applications. *Adv. Sci.* **2022**, *9*, 2103694.

[2] Wang, S. Y.; Zeng, R. H.; Ding, X. R.; Bai, H. S.; Zhu, X. L.; Jiang, H. W.; Zhou, R.; Tang, Y.; Li, H. Flexible triboelectric sensor array based on 3D printed bead-on-string sacrificial layer for human–machine interactions. *Nano Energy* **2024**, *122*, 109318.

[3] Jin, T.; Sun, Z. D.; Li, L.; Zhang, Q.; Zhu, M. L.; Zhang, Z. X.; Yuan,

G. J.; Chen, T.; Tian, Y. Z.; Hou, X. Y. et al. Triboelectric nanogenerator sensors for soft robotics aiming at digital twin applications. *Nat. Commun.* **2020**, *11*, 5381.

[4] Yao, C. J.; Liu, S. H.; Liu, Z. J.; Huang, S.; Sun, T. C.; He, M. Y.; Xiao, G. M.; Ouyang, H.; Tao, Y.; Qiao, Y. C. et al. Deep learning-enhanced anti-noise triboelectric acoustic sensor for human–machine collaboration in noisy environments. *Nat. Commun.* **2025**, *16*, 4276.

[5] Lin, Y. C.; Duan, S. S.; Zhu, D.; Li, Y. H.; Wang, B. H.; Wu, J. Self-powered and interface-independent tactile sensors based on bilayer single-electrode triboelectric nanogenerators for robotic electronic skin. *Adv. Intell. Syst.* **2023**, *5*, 2100120.

[6] Li, G.; Zhang, Y. R.; Zhang, X. L.; Zhu, B.; Lei, Y. F.; Chen, D. B.; Shui, L. Q.; Wu, G. Q.; Xue, L. J. Filiform papillae-inspired wearable pressure sensor with high sensitivity and wide detection range. *Adv. Funct. Mater.* **2025**, *35*, 2414465.

[7] Jose, M.; Vijjapu, M. T.; Neumaier, L.; Rauter, L.; Chakkunny, A. H.; Corzo, D.; Thoelen, R.; Picard, A.; Kosel, J.; Deferme, W. Convergence of biocompatible printed electronics and sensing in wound dressings: A leap forward in sustainable health monitoring. *npj Flex. Electron.* **2025**, *9*, 46.

[8] Han, C. C.; Cao, Z.; An, Z. Y.; Zhang, Z. W.; Wang, Z. L.; Wu, Z. Y. Multimodal finger‐shaped tactile sensor for multi-directional force and material identification. *Adv. Mater.* **2025**, *37*, 2414096.

[9] Chen, Z. F.; Wang, Z.; Li, X. M.; Lin, Y. X.; Luo, N. Q.; Long, M. Z.; Zhao, N.; Xu, J. B. Flexible piezoelectric-induced pressure sensors for static measurements based on nanowires/graphene heterostructures. *ACS Nano* **2017**, *11*, 4507–4513.

[10] Liu, Y. H.; Wang, J. L.; Liu, T.; Wei, Z. T.; Luo, B.; Chi, M. C.; Zhang, S.; Cai, C. C.; Gao, C.; Zhao, T. et al. Triboelectric tactile sensor for pressure and temperature sensing in high-temperature applications. *Nat. Commun.* **2025**, *16*, 383.

[11] Guo, M. J.; Xia, Y. F.; Liu, J. X.; Zhang, Y. H.; Li, M.; Wang, X. Wearable pressure sensor based on triboelectric nanogenerator for information encoding, gesture recognition, and wireless real-time robot control. *Adv. Funct. Mater.* **2025**, *35*, 2419209.

[12] Shu, S.; Wang, Z. M.; Chen, P. F.; Zhong, J. W.; Tang, W.; Wang, Z. L. Machine-learning assisted electronic skins capable of proprioception and exteroception in soft robotics. *Adv. Mater.* **2023**, *35*, 2211385.

[13] Zeng, W. H.; Ding, X. R.; Jin, Y.; Liu, B.; Zeng, R. H.; Gong, F.; Lou, Y.; Jiang, L. L.; Li, H. Magnetic soft millirobot with simultaneous locomotion and sensing capability. *npj Flex. Electron.* **2025**, *9*, 59.

[14] Kim, D.; Tcho, I. W.; Jin, I. K.; Park, S. J.; Jeon, S. B.; Kim, W. G.; Cho, H. S.; Lee, H. S.; Jeoung, S. C.; Choi, Y. K. Direct-laser-patterned friction layer for the output enhancement of a triboelectric nanogenerator. *Nano Energy* **2017**, *35*, 379–386.

[15] Zhang, T. T.; Wen, Z.; Lei, H.; Gao, Z. Q.; Chen, Y. F.; Zhang, Y.; Liu, J. Y.; Xie, Y. L.; Sun, X. H. Surface-microengineering for high-performance triboelectric tactile sensor via dynamically assembled ferrofluid template. *Nano Energy* **2021**, *87*, 106215.

[16] Liu, W. B.; Duo, Y.; Liu, J. Q.; Yuan, F. Y.; Li, L.; Li, L. C.; Wang, G.; Chen, B. H.; Wang, S. Q.; Yang, H. et al. Touchless interactive teaching of soft robots through flexible bimodal sensory interfaces. *Nat. Commun.* **2022**, *13*, 5030.

[17] Li, Y. F.; Zhang, S. W.; Gu, H. Y.; Li, Y. Y.; Zhao, H.; Huang, S. Q.; Feng, X. J.; Zhai, C. P.; Xu, M. L. Ultrasensitive piezoelectric-like film with designed cross-scale pores. *Sci. Adv.* **2025**, *11*, eadt4003.

[18] Huang, J.; Fu, X. P.; Liu, G. X.; Xu, S. H.; Li, X. W.; Zhang, C.; Jiang, L. Micro/nano-structures-enhanced triboelectric nanogenerators by femtosecond laser direct writing. *Nano Energy* **2019**, *62*, 638–644.

[19] Li, H.; Dong, X. R.; Jiang, H. W.; Qian, R. Z.; Wu, B.; Liu, B.; Jiang, L. L.; Tang, Y.; Ding, X. R. Wearable triboelectric nanogenerator with micro-topping structures via material jet printing method. *Nano Energy* **2023**, *114*, 108650.

[20] Chen, X. L.; Luo, Y. Z.; Chen, Y.; Li, S.; Deng, S. Z.; Wang, B.; Zhang, Q.; Li, X. M.; Li, X. M.; Wang, C. H. et al. Biomimetic contact behavior inspired tactile sensing array with programmable microdomes pattern by scalable and consistent fabrication. *Adv. Sci.* **2024**, *11*, 2408082.

[21] Trinh, V. L.; Chung, C. K. A facile method and novel mechanism using microneedle-structured PDMS for triboelectric generator applications. *Small* **2017**, *13*, 1700373.

[22] Chen, Z. P.; Ye, R.; Lee, W.; Jin, D. W.; Zhang, Y. X.; Jiang, L. Y.; Yang, Y. L.; Ren, L.; Jiang, L. L. Magnetization-induced self-assembling of bendable microneedle arrays for triboelectric nanogenerators. *Adv. Electron. Mater.* **2019**, *5*, 1800785.

[23] Yuan, Z. S.; Zhang, H. Z.; Hu, W. T.; Yu, X.; Qin, S.; Wang, C. Y.; Zhang, F. L. State-of-the-art review of metallic microneedles: Structure, fabrication, and application. *Chin. J. Mech. Eng.* **2025**, *38*, 21.

[24] Roh, H.; Yoon, Y. J.; Park, J. S.; Kang, D. H.; Kwak, S. M.; Lee, B. C.; Im, M. Fabrication of high-density out-of-plane microneedle arrays with various heights and diverse cross-sectional shapes. *Nano-Micro Lett.* **2022**, *14*, 24.

[25] Rad, Z. F.; Prewett, P. D.; Davies, G. J. Parametric optimization of two-photon direct laser writing process for manufacturing polymeric microneedles. *Addit. Manuf.* **2022**, *56*, 102953.

[26] Liu, Z. J.; Xu, X. Y.; Huang, S.; Huang, X. S.; Liu, Z. B.; Yao, C. J.; He, M. Y.; Chen, J. Y.; Chen, H. J.; Liu, J. et al. Multichannel microneedle dry electrode patches for minimally invasive transdermal recording of electrophysiological signals. *Microsyst. Nanoeng.* **2024**, *10*, 72.

[27] Gülçür, M.; Romano, J. M.; Penchev, P.; Gough, T.; Brown, E.; Dimov, S.; Whiteside, B. A cost-effective process chain for thermoplastic microneedle manufacture combining laser micro-machining and micro-injection moulding. *CIRP J. Manuf. Sci. Technol.* **2021**, *32*, 311–321.

[28] Sarkar, P.; Sidpara, A. M. Fabrication of microneedles using wire electric discharge machining and improving surface quality by electrochemical polishing. *J. Micromech. Microeng.* **2024**, *34*, 085008.

[29] An, Z. Y.; Wu, Z. Y.; Hu, Y. R.; Han, C. C.; Cao, Z.; Zhou, H. L.; Chen, Y. Y. A miniaturized array microneedle tactile sensor for intelligent object recognition. *Nano Energy* **2024**, *125*, 109567.

[30] Hu, Y. B.; Chatzilakou, E.; Pan, Z. S.; Traverso, G.; Yetisen, A. K. Microneedle sensors for point-of-care diagnostics. *Adv. Sci.* **2024**, *11*, 2306560.

[31] Li, H.; Wang, S. Y.; Dong, X. R.; Ding, X. R.; Sun, Y. N.; Tang, H.; Lu, Y. J.; Tang, Y.; Wu, X. Y. Recent advances on ink-based printing techniques for triboelectric nanogenerators: Printable inks, printing technologies and applications. *Nano Energy* **2022**, *101*, 107585.

[32] Li, H.; Fang, X. T.; Li, R. H.; Liu, B.; Tang, H.; Ding, X. R.; Xie, Y. X.; Zhou, R.; Zhou, G. F.; Tang, Y. All-printed soft triboelectric nanogenerator for energy harvesting and tactile sensing. *Nano Energy* **2020**, *78*, 105288.

[33] Zhang, Q. Y.; Li, J. H.; Li, G. Y.; Du, J. K.; Xie, C.; Li, H.; Jin, Y.; He, Y. Hierarchically structured hollow PVDF nanofibers for flexible piezoelectric sensor. *Chem. Eng. J.* **2024**, *498*, 155661.

[34] Li, X. J.; Shan, W. T.; Yang, Y.; Joralmon, D.; Zhu, Y. Z.; Chen, Y. Y.; Yuan, Y.; Xu, H.; Rong, J. H.; Dai, R. et al. Limpet tooth-inspired painless microneedles fabricated by magnetic field-assisted 3D printing. *Adv. Funct. Mater.* **2021**, *31*, 2003725.

[35] Qiao, H. Y.; Zhang, Y.; Huang, Z. G.; Wang, Y. M.; Li, D. Q.; Zhou, H. M. 3D printing individualized triboelectric nanogenerator with macro-pattern. *Nano Energy* **2018**, *50*, 126–132.

[36] Seol, M. L.; Woo, J. H.; Lee, D. I.; Im, H.; Hur, J.; Choi, Y. K. Nature-replicated nano-in-micro structures for triboelectric energy harvesting. *Small* **2014**, *10*, 3887–3894.

[37] Hu, X. Y.; Dong, X. R.; Li, Z. D.; Long, J. H.; Jin, Y.; Li, H. Numerical and experimental investigation of piezoelectric-pneumatic material jet printing method for high-viscosity ink. *Virtual Phys. Prototyping* **2025**, *20*, e2460210.

[38] Chen, L. F.; Shi, Q. F.; Sun, Y. J.; Nguyen, T.; Lee, C.; Soh, S.

Controlling surface charge generated by contact electrification: Strategies and applications. *Adv. Mater.* **2018**, *30*, 1802405.

[39] Li, M.; Yi, P.; Li, X.; Li, T.; Li, X.; Zhang, C.; Wang, Z.; Zhang, X.; Wang, A. *ACS Appl. Mater. Interfaces* **2025**.

[40] Seo, J.; Hajra, S.; Sahu, M.; Kim, H. J. Effect of cilia microstructure and ion injection upon single-electrode triboelectric nanogenerator for effective energy harvesting. *Mater. Lett.* **2021**, *304*, 130674.

[41] Xie, Y. B.; Hu, J. S.; Li, H.; Mi, H. Y.; Ni, G. L.; Zhu, X. S.; Jing, X.; Wang, Y. M.; Zheng, G. Q.; Liu, C. T. et al. Green fabrication of double-sided self-supporting triboelectric nanogenerator with high durability for energy harvesting and self-powered sensing. *Nano Energy* **2022**, *93*, 106827.

[42] Jiang, X. Z.; Sun, Y. J.; Fan, Z. Y.; Zhang, T. Y. Integrated flexible, waterproof, transparent, and self-powered tactile sensing panel. *ACS Nano* **2016**, *10*, 7696–7704.

[43] Ren, Z.; Nie, J.; Shao, J.; Lai, Q.; Wang, L.; Chen, J.; Chen, X.; Wang, Z. L. *Adv. Funct. Mater*. **2018**, *28*.

[44] Wang, L. Y.; Liu, Y. M.; Liu, Q.; Zhu, Y. Y.; Wang, H. Y.; Xie, Z. Q.; Yu, X. G.; Zi, Y. L. A metal-electrode-free, fully integrated, soft triboelectric sensor array for self-powered tactile sensing. *Microsyst. Nanoeng.* **2020**, *6*, 59.

[45] Zhu, Z.; Tian, Z.; Liu, Y.; Yue, S.; Li, Y.; Wang, Z. L.; Yu, Z. Z.; Yang, D. *Adv. Funct. Mater*. **2024**, *34*.

[46] Chen, H.; Wang, A. Q.; Chen, J.; Su, W. G.; Xu, X. Y.; Wang, J. B.; Li, X. D.; Meng, M.; Li, C.; Xu, C. H. et al. Drug-screening triboelectric nanogenerator-based strain sensor for cardiomyocyte contractility. *Nano Energy* **2023**, *109*, 108251.

[47] Wang, J. J.; Cui, P.; Zhang, J. J.; Ge, Y.; Liu, X. L.; Xuan, N. N.; Gu, G. Q.; Cheng, G.; Du, Z. L. A stretchable self-powered triboelectric tactile sensor with EGaIn alloy electrode for ultra-low-pressure detection. *Nano Energy* **2021**, *89*, 106320.

[48] Tian, X.; Niu, B.; Hua, T.; Yang, M. Y.; Yang, Y. Y.; Dong, S. S. Continuous fabrication of a highly integrated, user-friendly, and low-cost triboelectric yarn/fabric for diverse sensing applications. *ACS Sustainable Chem. Eng.* **2023**, *11*, 16087–16097.

[49] Zhong, Y.; Wang, J. Q.; Wu, L. G.; Liu, K. S.; Dai, S. P.; Hua, J.; Cheng, G. G.; Ding, J. N. Dome-conformal electrode strategy for enhancing the sensitivity of $BaTiO_3$-doped flexible self-powered triboelectric pressure sensor. *ACS Appl. Mater. Interfaces* **2024**, *16*, 1727–1736.

[50] Park, J.; Kim, I.; Yun, J.; Kim, D. Liquid-metal embedded sponge-typed triboelectric nanogenerator for omnidirectionally detectable self-powered motion sensor. *Nano Energy* **2021**, *89*, 106442.

[51] Zhao, Z. Z.; Huang, Q. Y.; Yan, C.; Liu, Y. D.; Zeng, X. W.; Wei, X. D.; Hu, Y. F.; Zheng, Z. J. Machine-washable and breathable pressure sensors based on triboelectric nanogenerators enabled by textile technologies. *Nano Energy* **2020**, *70*, 104528.

[52] Zu, L. L.; Wen, J.; Wang, S. B.; Zhang, M.; Sun, W. L.; Chen, B. D.; Wang, Z. L. Multiangle, self-powered sensor array for monitoring head impacts. *Sci. Adv.* **2023**, *9*, eadg5152.

[53] Hu, J.; Liu, Z. Q.; Yang, P.; Qin, S. Y.; Li, N.; Ji, W. Y.; Wang, Z. L.; Chen, X. Y. Charge transfer behavior of triboelectric polymers and triboelectric sensors operated under ultrahigh pressure. *SusMat* **2024**, *4*, e250.

[54] Liu, Z.; Ma, Y.; Ouyang, H.; Shi, B. J.; Li, N.; Jiang, D. J.; Xie, F.; Qu, D.; Zou, Y.; Huang, Y. et al. Transcatheter self-powered ultrasensitive endocardial pressure sensor. *Adv. Funct. Mater.* **2019**, *29*, 1807560.

[55] Qin, S. Y.; Yang, P.; Liu, Z. Q.; Hu, J.; Li, N.; Ding, L. M.; Chen, X. Y. Triboelectric sensor with ultra-wide linear range based on water-containing elastomer and ion-rich interface. *Nat. Commun.* **2024**, *15*, 10640.

[56] Lee, E. I.; Ko, H. J.; Kim, J.; Park, J. W. Self-powered single multifunctional tactile sensor for simultaneous detection of dynamic and static pressure and temperature inspired by skin sensory functions. *Nano Energy* **2025**, *139*, 110984.

[57] Ma, M. Y.; Zhang, Z.; Zhao, Z. N.; Liao, Q. L.; Kang, Z.; Gao, F. F.; Zhao, X.; Zhang, Y. Self-powered flexible antibacterial tactile sensor based on triboelectric-piezoelectric-pyroelectric multi-effect coupling mechanism. *Nano Energy* **2019**, *66*, 104105.

[58] Bai, P.; Zhu, G.; Jing, Q. S.; Yang, J.; Chen, J.; Su, Y. J.; Ma, J. S.; Zhang, G.; Wang, Z. L. Membrane-based self-powered triboelectric sensors for pressure change detection and its uses in security surveillance and healthcare monitoring. *Adv. Funct. Mater.* **2014**, *24*, 5807–5813.

[59] Ke, K. H.; Chung, C. K. High-performance Al/PDMS TENG with novel complex morphology of two-height microneedles array for high-sensitivity force-sensor and self-powered application. *Small* **2020**, *16*, 2001209.

[60] Ji, B.; Zhou, Q.; Hu, B.; Zhong, J. W.; Zhou, J.; Zhou, B. P. Bio-inspired hybrid dielectric for capacitive and triboelectric tactile sensors with high sensitivity and ultrawide linearity range. *Adv. Mater.* **2021**, *33*, 2100859.

[61] Wang, J. X.; Ma, L. L.; He, J. M.; Yao, Y. L.; Zhu, X. D.; Peng, L.; Yang, J.; Li, K. S.; Qu, M. N. Superwettable hybrid dielectric based multimodal triboelectric nanogenerator with superior durability and efficiency for biomechanical energy and hydropower harvesting. *Chem. Eng. J.* **2022**, *431*, 134002.

[62] Sun, R. X.; Wu, P. F.; Li, P.; Jiang, J. C.; Shou, M. J.; Chen, Q.; Yang, P. G.; Wang, F. Y.; Liao, C. R. Bio-inspired triboelectric nanogenerator as a self-powered gait recognition sensor for legged robots. *Sci. China Mater.* **2025**, *68*, 1542–1551.